ACSNANO

www.acsnano.org

ARTICLE

Tuning of the Aggregation Behavior of Fluorinated Polymeric Nanoparticles for Improved Therapeutic Efficacy

Cheng Zhang,* Tianqing Liu, Wenqian Wang, Craig A. Bell, Yanxiao Han, Changkui Fu, Hui Peng, Xiao Tan, Petr Král, Katharina Gaus, J. Justin Gooding, and Andrew K. Whittaker*

Cite This: *ACS Nano* 2020, 14, 7425−7434

Read Online

ACCESS | Metrics & More | Article Recommendations | Supporting Information

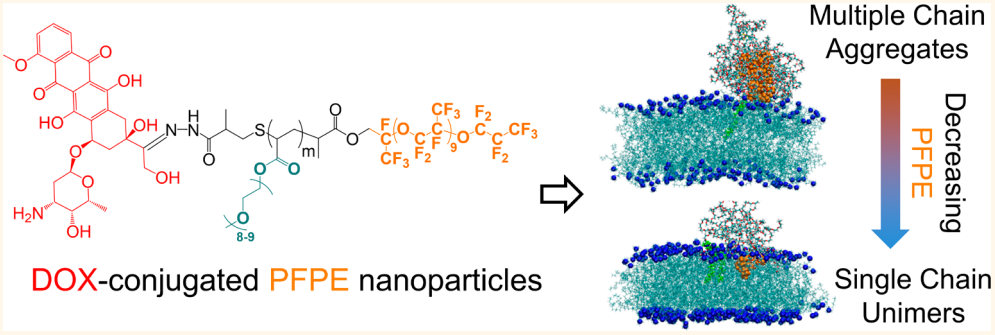

ABSTRACT: **Incorporation of fluorinated moieties in polymeric nanoparticles has been shown in many instances to increase their uptake by living cells and, hence, has proven to be a useful approach to enhancing delivery to cells. However, it remains unclear how incorporation of fluorine affects critical transport processes, such as interactions with membranes, intracellular transport, and tumor penetration. In this study, we investigate the influence of fluorine on transport properties using a series of rationally designed poly(oligo(ethylene glycol) methyl ether acrylate)-*block*-perfluoropolyether (poly(OEGA)$_m$-PFPE) copolymers. Copolymers with different fluorine contents were prepared and exhibit aggregate in solution in a manner dependent on the fluorine content. Doxorubicin-conjugated poly(OEGA)$_{20}$-PFPE nanoparticles with lower fluorine content exist in solution as unimers, leading to greater exposure of hydrophobic PFPE segments to the cell surface. This, in turn, results in greater cellular uptake, deeper tumor penetration, as well as enhanced therapeutic efficacy compared to that with the micelle-state nanoaggregates (poly(OEGA)$_{10}$-PFPE and poly(OEGA)$_5$-PFPE) with higher fluorine content but with less PFPE exposed to the cell membranes. Our results demonstrate that the aggregation behavior of these fluorinated polymers plays a critical role in internalization and transport in living cells and 3D spheroids, providing important design criteria for the preparation of highly effective delivery agents.**

KEYWORDS: *fluorine, nanoparticles, polymers, nanomedicines, drug delivery, breast cancer*

Despite being absent in most biological systems, fluorine has been widely used to tailor the properties and behavior of molecules and particles for biomedical applications.[1−4] The substitution of hydrogen with fluorine can improve cellular uptake and subsequently facilitate the crossing of intracellular bilayers, thus increasing the therapeutic efficacy of certain drugs.[2,5−12] Molecules containing fluorine have hydrophobic and lipophobic characteristics and tend to form aggregates in aqueous solutions. As such, long-term stability and well-controlled aggregation under physiological conditions are significant challenges.[13−15] For example, high contents of fluorine may facilitate enhanced cellular uptake but can lead to low stability in aqueous solutions and the formation of large aggregates. These aggregates are expected to significantly influence cell membrane affinity. Such behavior may not be desirable for controlled delivery of therapeutic agents.

Received: April 7, 2020
Accepted: May 13, 2020
Published: May 13, 2020

https://dx.doi.org/10.1021/acsnano.0c02954
ACS Nano 2020, 14, 7425−7434

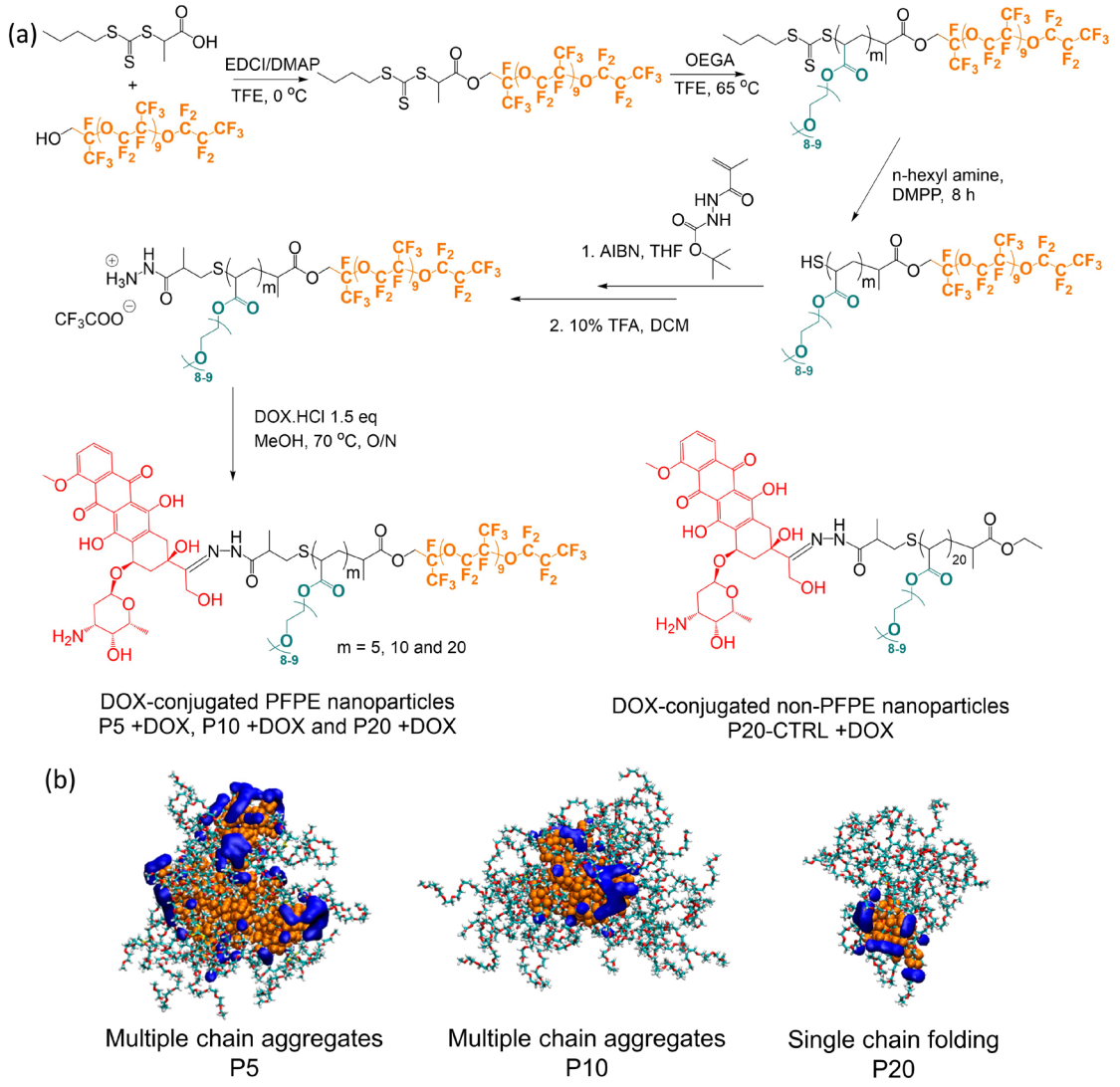

Figure 1. (a) Synthetic scheme describing preparation of DOX-loaded PFPE nanoparticles with $m = 5$ (P5 + DOX, $F = 28.7$ wt %), $m = 10$ (P10 + DOX, $F = 17.0$ wt %), and $m = 20$ (P20 + DOX, $F = 9.8$ wt %) OEGA repeat units. The non-PFPE control polymer (P20-CTRL + DOX) with 20 OEGA repeating units was prepared as a control. (b) Aggregation states of PFPE nanoparticles in 150 mM NaCl solution. Snapshots of the MD simulations were taken at the end of 20 ns (the nanoaggregates contain eight and four polymer chains for P5 and P10, respectively, and one for P20). PFPE segments are shown in orange, and the hydrophilic OEGA parts are in atomistic detail. The PFPE segments exposed to the solution, defined as segments having water molecules within 3 Å, are labeled in blue.

In previous studies, a range of fluorinated delivery agents have been reported, including fluorinated oligonucleotides with potential antisense activity and fluorinated lipid constructs for enhanced transport and uptake.[4,9,16−18] Metelev *et al.* reported the synthesis of fluorocarbon-based oligodeoxynucleotide duplexes (ODND) and explored the role of fluorocarbons in enhancing cellular uptake and intracellular delivery. The authors reported that modification with fluorocarbons resulted in a 2- to 4-fold increase in cellular uptake compared to unmodified ODND as determined by quantitative confocal fluorescence imaging of A431 and INS-1 cells.[1] The high affinity of fluorinated moieties with cell membranes is believed to facilitate enhanced endocytic uptake.[2,6,19,20] However, these reports are not focused on the mechanism of enhanced uptake induced by the presence of hydrophobic fluorine. Indeed, studies of solution behavior of these fluorinated molecules and nanoparticles, including serum stability and aggregation, are largely absent from the literature.

In this contribution, we prepare a series of fluorinated polymeric nanoparticles containing perfluoropolyether (PFPE) as the fluorinated, hydrophobic segment and oligo(ethylene glycol) methyl ether acrylate (OEGA) as the hydrophilic monomer through reversible addition−fragmentation chain-transfer (RAFT) polymerization (Figure 1a). These nanoparticles have well-controlled aggregation behavior in solution, and depending on the fluorine content, multiple-chain nanoaggregates or single-chain folded nanoparticles can be formed.[21−24] A combination of experimental and computational techniques was employed to investigate how the aggregation behavior of these PFPE-containing nanoparticles affects their cellular uptake, intracellular transport, 3D spheroid penetration, and finally their therapeutic efficacy. Our results suggest that fluorinated polymeric nanoparticles undergoing a single-chain folding conformation (lower fluorine content) have a larger proportion of hydrophobic PFPE segments exposed to the cell surface, providing significantly improved drug delivery efficiency to living cells and to the center of 3D spheroids, resulting in

https://dx.doi.org/10.1021/acsnano.0c02954
ACS Nano 2020, 14, 7425−7434

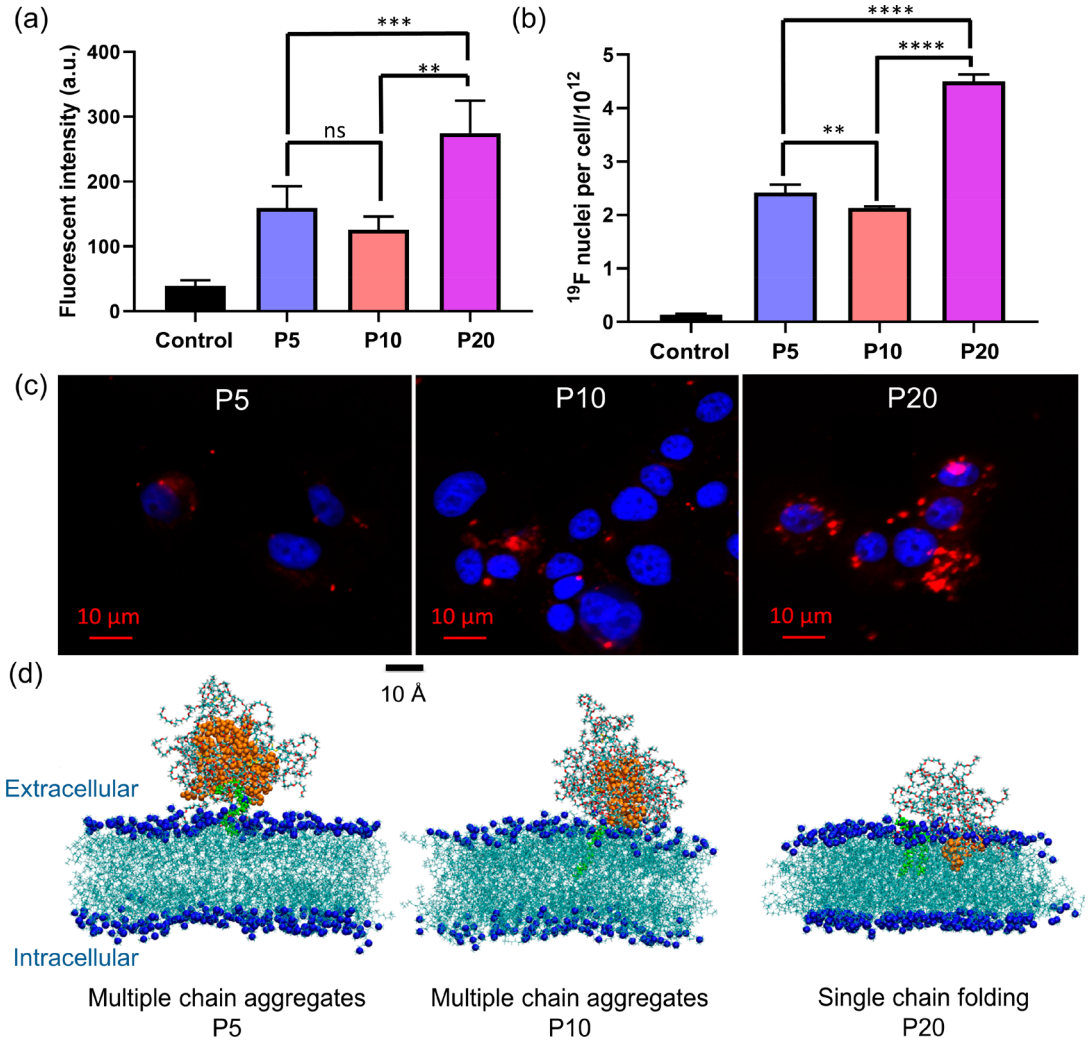

Figure 2. Cellular uptake of PFPE nanoparticles in MCF-7 breast cancer cells measured by (a) flow cytometry, based on the detection of fluorescence intensity per cell, and (b) ^{19}F NMR spectroscopy, based on the quantification of the ^{19}F NMR signal intensity per cell. Experiments were performed in triplicate to obtain mean and standard deviation values (shown as error bars); ns, not significant; $p > 0.05$; $^{**}p < 0.01$; $^{***}p < 0.001$, $^{****}p < 0.0001$ (t test). The total cell number was determined using a hemocytometer with Trypan blue exclusion. (c) Confocal microscopy of MCF-7 cells incubated with Cy5.5-labeled PFPE nanoparticles (red) at same dye concentration (0.25 mM) for 24 h at 37 °C. Cell nuclei were counterstained with DAPI (blue). (d) Snapshots taken at 40 ns of MD simulation indicate faster penetration of P20 (single-chain unimers, right) than P5 (multiple-chain nanoaggregates, left) and P10 (multiple-chain nanoaggregates, middle) across the cell membrane. The PFPE segments are orange, the cell membrane is shown in dark and light blue, and green designates the protrusion of membrane.

enhanced therapeutic efficacy. The study describes opportunities for the design and preparation of highly efficient fluorinated delivery agents.

RESULTS AND DISCUSSION

Preparation of Doxorubicin-Conjugated PFPE Nanoparticles with Controlled Aggregation Behavior. A series of amphiphilic water-soluble fluorinated polymers with fluorine contents from 9.8, 17.0, and 28.7 wt % were prepared (Figure 1a), and designated *Pm*, i.e. P20, P10 and P5, with the suffix denoting the number-average degree of polymerization of the OEGA segments. The aggregation behavior of the polymers from multiple-chain aggregation to single-chain folding was investigated by means of dynamic light scattering (DLS), high-resolution NMR, and molecular dynamics (MD) simulations. The hydrodynamic diameters (D_h) of the PFPE nanoparticles determined by DLS were similar (8.1, 9.3, and 8.3 nm for P5, P10, and P20, respectively, Table S1), regardless of molecular weight, indicating differences in aggregation behavior of polymers with different PFPE contents—this is supported by the results of MD simulations (see Figure 1b). From these analyses, we conclude that poly(OEGA)$_{20}$-PFPE (P20) undergoes single-chain folding, whereas poly(OEGA)$_{10}$-PFPE (P10) and poly(OEGA)$_5$-PFPE (P5) form multiple-chain nanoaggregates in aqueous solution (Figure 1b).[21] Detailed structural characteristics of the polymeric nanoparticles can be found in Figures S1 and S2 and Table S1. It should be noted that the dispersity in molecular weight ($Đ$) can have a great influence on self-assembly;[25] however, in this study, all PFPE polymers had a low dispersity at 1.08, and the effect of $Đ$ on aggregation behavior is thus assumed to be largely negligible. The nature of the aggregation of the polymeric chains results in different extents of exposure of the hydrophobic PFPE segments to the solution and hence potentially to the surface of cells in solution. The polymeric assemblies are therefore expected to have different affinities for cellular membranes and different drug

https://dx.doi.org/10.1021/acsnano.0c02954
ACS Nano 2020, 14, 7425−7434

delivery efficiencies.[2,7,16] For comparison, polymers lacking the fluorinated segment (P20-CTRL) were prepared by replacing the PFPE segments with nonfluorinated aliphatic ethyl groups. The nonfluorinated OEGA-based polymers are less hydrophobic than the fluorine-bearing chains and therefore exist as unimers in aqueous solution (Figure 1a and Figure S3 and Table S1).

Doxorubicin (DOX) is a widely reported anticancer drug effective on several types of cancer including breast cancer.[26−28] DOX is a fluorescent molecule and therefore is suitable for *in vitro* imaging studies. The sterically unhindered ketone functionality of DOX allows for the attachment to the fluorinated copolymers *via* a pH-dependent hydrolytically degradable hydrazone bond without the need for further modification.[29] To facilitate attachment to the polymer chains, the trithiocarbonate end groups of the polymer were first reduced to thiols in the presence of hexylamine. The thiol end groups were then conjugated with Boc-protected hydrazide methacrylate (TBMC) through the Michael addition reaction, followed by deprotection of the Boc group (Figure S4). Refluxing the polymers with attached hydrazide groups in methanol with DOX (1.5 equiv of DOX to hydrazides) and a catalytic amount of glacial acetic acid resulted in DOX-loaded polymers through the formation of hydrazone linkages.[30] The polymers were then extensively purified by dialysis at pH 8 to remove free DOX molecules, and the DOX loading of each polymer was calculated to be 13.5, 8.5, 4.9, and 6.3 wt % for P5 + DOX, P10 + DOX, P20 + DOX, and P20-CTRL + DOX, respectively.

Dependence of Cellular Uptake on Aggregation Behavior. Polymeric nanoparticles were incubated with MCF-7 breast cancer cells at 37 °C to assess the effect of aggregation on cellular uptake. The study was conducted utilizing both experimental and computational experiments, including flow cytometry, ^{19}F NMR spectroscopy, confocal microscopy, as well as MD simulations. As described above, polymers P5 and P10 form multiple-chain aggregates in solution, whereas P20 exists as a unimer in a single-chain folded state. ^{19}F NMR measurements confirmed no obvious line broadening, attenuation of signal, or changes in self-diffusion coefficient in the presence of 10% fetal bovine serum in phosphate-buffered saline (PBS) (Figure S5 and Table S1). Therefore, it is concluded that the aggregation state of the PFPE polymers in cell culture medium should be the same as that in buffered solution.

The results obtained using flow cytometry show that all three Cy5.5-conjugated PFPE nanoparticles are extensively taken up by MCF-7 cells. The P20 single-chain unimers with the largest extent of exposure of hydrophobic PFPE segments showed the highest uptake after 24 h incubation (Figure 2a). Quantitative ^{19}F NMR measurements were also conducted to examine the intracellular fluorine concentration. This was achieved by comparing the intensity of the ^{19}F NMR spectrum of the nanoparticles incubated with the cells with a reference standard (trifluoroacetic acid, TFA, $\delta = -76.5$ ppm, Figure S6). After cell lysis, the most intense peak in the ^{19}F NMR spectrum was observed at approximately −82 ppm, assigned to the fluorinated methyl and methylene chemical groups of the PFPE segments (peak F1 in Figure S2). Using the method reported by Ahrens and co-workers,[31,32] the fluorine content in each cell was determined as $(2.58 \pm 0.15) \times 10^{10}$, $(2.16 \pm 0.03) \times 10^{10}$m and $(4.49 \pm 0.13) \times 10^{10}$ fluorine spins for P5, P10, and P20, respectively (Figure 2b). The results of these intracellular ^{19}F NMR measurements are consistent with the results obtained from flow cytometry. In addition, intracellular ^{19}F NMR properties were examined without cell lysis (Figure S7). An intense ^{19}F NMR signal with reasonable ^{19}F transverse and longitudinal relaxation times (T_2 and T_1, respectively) were observed for all cases, implying potential for applying these PFPE nanoparticles in image-guided therapeutics.[33] It should be noted that the P20 polymer has the highest segmental mobility (longest ^{19}F T_2) for intracellular ^{19}F magnetic resonance imaging.

The uptake of Cy5.5-labeled PFPE nanoparticles by MCF-7 cells after exposure for 24 h was visualized using confocal microscopy. The *Z*-slices through the center of the cells clearly show red staining, indicating localization of the PFPE nanoparticles within the cell body (Figure 2c). The confocal images show stronger red fluorescence and, hence, greater extent of uptake of P20 single-chain unimers compared to P5 and P10, agreeing well with the observations by flow cytometry and ^{19}F NMR analysis (Figure 2a,b). These results confirm that P20 is taken up most efficiently, and that the extent of uptake of the polymers correlates with the proportion of PFPE segments exposed in an aqueous solution.

Atomistic MD simulations were conducted to assist with the interpretation of the experimental observations.[34−36] The snapshots of the simulations in Figure S8a−c show the aggregation states of P5, P10, and P20 in 150 mM NaCl solution after 20 ns of simulation. These results are consistent with our experimental findings and further confirm that the P5 and P10 nanoaggregates can form micelle-like assemblies (eight and four polymer chains for P5 and P10, respectively), with the OEGA side chains within the shell and the PFPE blocks constituting the core. In contrast, the P20 adopts a single-chain folded conformation, indicating that the longer OEGA segment is able to stabilize a single fluorocarbon block. A biological membrane, consisting of a phosphatidylcholine (POPC) bilayer with stochastic protrusion of an aliphatic lipid tail into solution, was simulated under the same conditions.[37,38] PFPE nanoparticles were then placed within 5 Å of the membrane, and simulation of the whole system was performed (Figure S8d−f). Over the time course of 40 ns simulations, interactions between PFPE nanoparticles and the cell membrane were recorded. The proportion of hydrophobic PFPE and hydrophilic PEG segments exposed to the cell membrane (within 3 Å distance) was calculated to be 10.8, 11.3, and 13.3% for P5, P10, and P20, respectively. At 40 ns, the nanoparticles of P5 and P10 moved toward and stably settled on the surface of the membrane without noticeable changes in conformation, whereas the P20 single-chain unimers with more hydrophobic PFPE segments exposed to the cell membrane were observed to insert and fuse within the lipid membrane (Figure 2d), presumably due to stronger hydrophobic interactions with the exposed lipid tail. We should also note that P20 has a much smaller hydrophobic core (one PFPE chain per nanoparticle) compared with P5 and P10 with eight and four PFPE chains per nanoparticle, respectively, leading to faster diffusion across barriers of cell membrane. These simulation results further support the experimental observations and highlight how exposure of hydrophobic PFPE segments to the cell surface can promote interactions with membranes and hence enhance uptake. The simulations also illustrate that a critical step to initiate cellular uptake is the hydrophobic−hydrophobic contact between the fluorinated segments and the lipid chains, and that stochastic protrusion of an aliphatic lipid tail of the bilayer into the solution

https://dx.doi.org/10.1021/acsnano.0c02954
ACS Nano 2020, 14, 7425−7434

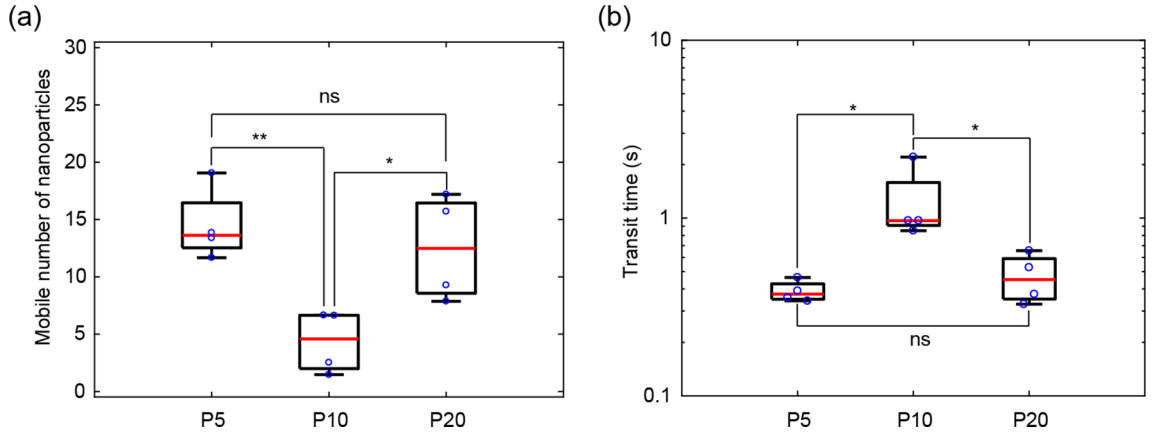

Figure 3. Auto- and pair-correlation microscopy analysis of the movement of PFPE nanoparticles inside the cytoplasm. (a) Mobile number of PFPE nanoparticles with different extents of PFPE exposure tracked by the scanning line inside the cytoplasm. (b) Transit times of PFPE nanoparticles with different PFPE exposures moving along the direction of scanning line for 1.2 μm; ns, not significant; $p > 0.05$; *$p < 0.05$; **$p < 0.01$ (one-way ANOVA).

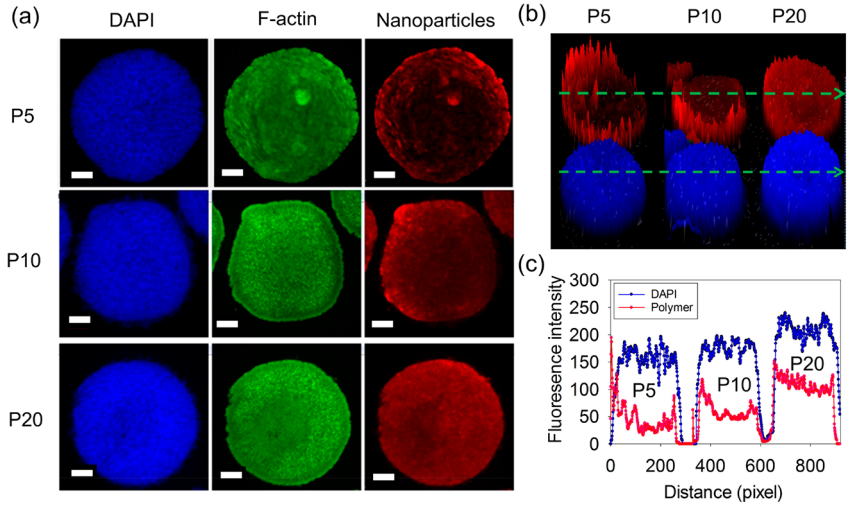

Figure 4. P20 single-chain unimers penetrates into the tumor spheroids more effectively than the P5 and P10 nanoaggregates. P5, P10, and P20 at the same concentration (0.25 mM) were incubated with 3D MCF-7 tumor spheroids for 24 h at 37 °C. (a) Confocal images of tumor spheroids at different channels (DAPI = blue, F-actin = green, polymer = red) for P5, P10, and P20. (b) Surface plots of images shown in (a) produced in ImageJ. (c) Fluorescence intensity profiles of tumor spheroids treated with PFPE nanoparticles clearly show the enhanced penetration of the P20. Scale bars are 100 μm.

is important. Interactions between PFPE nanoparticles and cell membranes were not observed within the simulation time frame for membranes without lipid tail protrusion (Figure S9). A similar observation was reported by Van Lehn *et al.* in their studies of insertion of gold nanoparticles into model cell membranes.[38]

Intracellular Transport of PFPE Nanoparticles. The intracellular transport of the PFPE nanoparticles was studied using auto- and pair-correlation microscopy. These methods allow quantitative measurement of two important parameters related to the polymer aggregation state: (1) the local number of mobile nanoparticles and (2) the rate of diffusion of nanoparticles in the cytoplasm. MCF-7 breast cancer cells were incubated with PFPE nanoparticles for 4 h at 37 °C. A continuous line scan of fluorescence intensity was performed using confocal microscopy, spanning from the extracellular space to the nucleus of the cell under examination. The number of mobile nanoparticles at each pixel on the line scan could be determined from the autocorrelation function. Transit times of nanoparticles moving within a certain distance were obtained from the pair-correlation function. More details of the analysis are provided in the Supporting Information and in our previous reports.[22,39]

The intracellular distributions of the nanoparticles in MCF-7 cells (Supporting Information Figure S10) suggest that, after 4 h of incubation, all three nanoparticles (P5, P10, and P20) are located mainly in the cytoplasm rather than in the nucleus. Figure 3a shows the number of mobile P5 and P20 nanoparticles (14.5 and 12.5 nanoparticles per pixel) in the cytoplasm calculated from the autocorrelation function, values which are significantly higher that of than P10 (4.3 nanoparticles per pixel). This is related to the much higher levels of cellular uptake of the P20 single-chain unimers, as discussed in the previous section. A larger number of intracellular mobile nanoparticles are observed for P5 than P10—this may be due to the slightly higher cell uptake and smaller aggregated size of P5 (Table S1 and Figure 2a,b). The diffusion coefficients of PFPE nanoparticles moving in the cytoplasm can also be calculated from an

https://dx.doi.org/10.1021/acsnano.0c02954
ACS Nano 2020, 14, 7425−7434

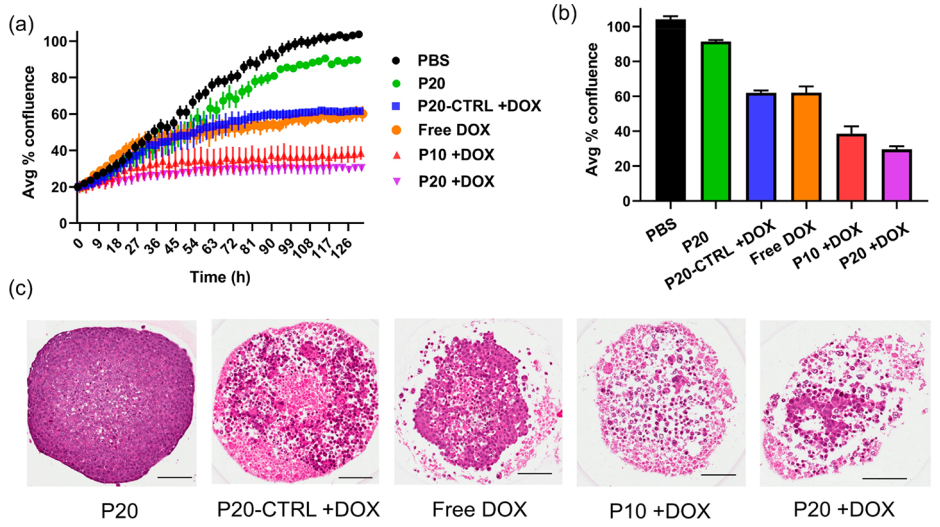

Figure 5. Inhibition of cell proliferation of 2D monolayer culture as well as the morphological and histological examination of MCF-7 tumor spheroids. Cell proliferation was monitored in real-time with the continuous presence of indicated treatments until the end of each experiment. The changes in cell confluence were used as a surrogate marker of cell proliferation. (a) Changes in cell confluence with incubation time for 144 h. (b) Cell confluence at 144 h incubation time. Data shown in (a,b) are the mean ± SD (n = 6). Cell proliferation was assessed by confluence measurements using IncuCyte. (c) Representative images of H&E stained paraffin sections of MCF-7 tumor spheroids incubated with P20 without conjugation of DOX (P20), nonfluorinated control polymer with DOX (P20-CTRL + DOX), free DOX, P10 nanoaggregates with DOX (P10 + DOX), and P20 single-chain unimers with DOX (P20 + DOX). Bar = 100 μm.

autocorrelation function: 1.19 ± 0.19, 0.23 ± 0.16, and 0.74 ± 0.26 $\mu m^2/s$ for P5, P10, and P20, respectively (Figure S11). These intracellular diffusion coefficients of PFPE nanoparticles are approximately 100 times smaller than those for the PFPE nanoparticles in pure water (Table S1). It has been reported that the viscosity of cytoplasmic fluid is slightly higher than that of pure water (1−2 cP and 0.89 at 25 °C for the aqueous phase of cytoplasm and water, respectively);[40,41] therefore, such slow rates of diffusion may arise in part from collisions with large macromolecules within the cytosol.[42−45] The diffusion data also indicate that the mobility of P5 and P20 in the cytoplasm is significantly higher than that of P10. Note that P5 has the largest diffusion coefficient, indicating the possibility of disassembly into unimers during the cell internalization process, whereas the P10 nanoaggregates with more hydrophilic OEG segments in the shell were present as micelles having the slowest intracellular diffusion.

Subsequently, the pair correlation function was used to measure the transit times of PFPE nanoparticles within the cytoplasm at a distance (δr) = 1.2 μm. It can be seen in Figure 3b that the transit times of P5 and P20 within the cytoplasm on moving a distance of 1.2 μm (0.39 ± 0.054 and 0.47 ± 0.15 s for P5 and P20, respectively) were significantly shorter than that of P10 (1.25 ± 0.64 s). The longer transit time for the P10 nanoparticles is consistent with the P10 nanoaggregates (9.3 nm) being slightly larger than the P5 and P20 (8.1 and 8.3 nm, respectively, Table S1).

Penetration of PFPE Nanoparticles into 3D Tumor Spheroids. The capacity of the PFPE nanoparticles to penetrate 3D cellular structures was examined by exposing MCF-7 tumor spheroids to solutions of the nanoparticles. Compared with conventional monolayer cell cultures, 3D tumor spheroids are proposed to be a better mimic of the microenvironment of vascular tumor tissues due to the abundant cell−cell and cell−matrix interactions with the 3D tissue structure.[46] The size of the MCF-7 tumor spheroids was monitored until it reached the desired value (~500 μm in diameter), and PFPE nanoparticles were then added and incubated with the spheroids for 24 h at 37 °C before being washed with PBS buffer to remove free nanoparticles.

The location of Cy5.5-conjugated nanoparticles within the MCF-7 spheroids was determined by confocal microscopy, and the results are shown in red in Figure 4a. It can be concluded that the P20 single-chain unimers can more readily penetrate throughout the center of the 3D tumor spheroids as opposed to the P5 and P10 nanoaggregates (Figure 4b,c). It has been reported that trafficking of molecules inside spheroids is mainly dependent on two pathways: transcellular transport and diffusion through the extracellular matrix networks between the cells.[47,48] To be more specific, the penetration pathway *via* transcellular transport is highly dependent on the intracellular concentration of nanoparticles, and this is because higher intracellular concentrations would lead to a higher probability of nanoparticles escaping from cells *via* exocytosis. Therefore, compared with the P5 and P10 nanoaggregates, P20 single-chain unimers with much higher cellular uptake is expected to exhibit higher penetration capacity throughout the 3D spheroid model.

Therapeutic Efficacy of DOX-Conjugated PFPE Nanoparticles. Cell proliferation assays were performed by monitoring real-time changes in the percentage confluence of MCF-7 cells over 6 days using a 2D monolayer culture model. In comparison with PBS controls, there was negligible effect of the P20 without DOX (P20) on MCF-7 cell growth (Figure 5a). Treatment with either DOX-loaded nanoparticles or free DOX showed effective inhibition of the proliferation of MCF-7 cells. The DOX-loaded nonfluorinated control polymer (P20-CTRL + DOX) behaved similarly to free DOX. However, the incorporation of PFPE segments resulted in an approximately 2-fold reduction in cell numbers (P10 + DOX and P20 + DOX, Figure 5a,b), and notably, the DOX-loaded P20 single-chain unimers exhibited inhibition significantly stronger than that of the DOX-loaded P10 nanoaggregates (38.7 and 29.6% for P10 + DOX and P20 + DOX, respectively). This is ascribed to the DOX-loaded P20 having higher cellular uptake and faster

https://dx.doi.org/10.1021/acsnano.0c02954
ACS Nano 2020, 14, 7425−7434

intracellular diffusion than the DOX-loaded P10 nanoaggregates. These properties lead to improved DOX delivery to MCF-7 cells. Note that the DOX-loaded P5 nanoaggregates are not well dissolved in the cell culture medium, and no inhibition data were acquired for P5. Instead of using our current strategy by directly dissolving P5 in culture medium, stable P5 nanoaggregates could be generated by first dissolving the polymer in dimethyl sulfoxide and then mixing with culture medium.

The anticancer therapeutic efficacy of DOX-conjugated PFPE nanoparticles was also assessed in 3D cell culture by histological analysis of the MCF-7 spheroids (Figure 5c). Tumor spheroids with an average diameter of ~400−500 μm were exposed to several different types of DOX-loaded nanoparticles (1 μM DOX). Similar to the analysis of cell proliferation assays, the P20 without conjugation of DOX had little to no effect on the spheroid structure and cell viability in the spheroids. Spheroids exposed to P20-CTRL + DOX and free DOX exhibited obvious cell death in the outer region of the spheroids, but it should be noted that the spheroid structure was well maintained after treatment with the nanoparticles. In contrast, P10 + DOX and P20 + DOX caused obvious cell death and tissue damage throughout the tumor spheroids, and the spheroid structure was destroyed after incubation with the P20 + DOX single-chain unimers, which again is likely due to its high cellular uptake and tissue penetration. The promising results based on both 2D and 3D cellular models indicated a much improved anticancer therapeutic effect could be achieved by the incorporation of PFPE segments. In addition, increasing the exposure of hydrophobic PFPE segments to solution by carefully changing the hydrophobic/hydrophilic balance could enhance DOX delivery to cells located on both the surface and at the center of tumor spheroids and can further accelerate the anticancer therapeutic efficiency. The results gained from this study provide important design criteria to optimize the structure of fluorinated polymers for design of highly efficient drug delivery agents.

CONCLUSIONS

We report the use of a polymeric PFPE-based platform to examine how aggregation behavior affects interactions between fluorinated nanoparticles and living cells at the molecular level. P20 nanoparticles in the form of unimers contain fewer hydrophobic PFPE segments, but these are more extensively exposed to the solution and hence to the cell surface on encountering cells. The P20 single-chain unimers show an approximately 2-fold higher uptake by MCF-7 cells, more extensive penetration into 3D MCF-7 tumor spheroids, and higher therapeutic efficacy compared to the P5 and P10 nanoaggregates which form micelles. After internalization by the cells, P5 and P20 showed intracellular diffusion significantly faster than that of P10, due in part to the larger size of aggregates of P10. The investigations obtained from this study provide important design criteria for effective fluorinated molecular transporters: higher extent of exposure of fluorinated segments and smaller size of fluorinated core are beneficial for maximizing delivery efficiency.

EXPERIMENTAL SECTION

^{19}F NMR Analysis of Cellular Uptake. The cellular uptake of the polymer was determined by ^{19}F NMR spectroscopy. In order to obtain a relatively strong ^{19}F NMR signal from the polymer in cells, a large number of cells was required, and cells were therefore grown in a T175 flask with a polymer concentration at 10 mg/mL. The cell number was determined using a hemocytometer with Trypan blue exclusion (≈5 × 10^6 cells in each case). Cells of a known number were placed in 200 μL of Triton lysis buffer (diluted in deuterium oxide, 1%) and mixed with 80 μL of ^{19}F standard of TFA (0.1%).

^{19}F NMR spectra of the solutions were acquired with a relaxation delay of 10 s, and the number of scans was 512.

Two distinct peaks were observed at −76.55 ppm for TFA and −82 ppm for the PFPE-based polymers (Figure S6). The mean number of ^{19}F nuclei per cell was calculated using the following formula:

$$F_c = \frac{3I_s M_r N_a}{I_r N_c}$$

where the I_s is the integrated area of major peak of the cell pellet, M_r is moles of TFA reference, N_a is Avogadro's number, I_r is the integrated area under the TFA reference peak, and N_c is the number of cells in pellet.

Intracellular ^{19}F NMR Analysis. The in-cell ^{19}F NMR properties of the PFPE-based polymers were measured using a Bruker Avance 400 MHz spectrometer. Cells in four T175 flasks (≈2 × 10^7 cells) were cultured with the polymer at a concentration of 10 mg/mL for 24 h and then fixed with 4% paraformaldehyde (PFA) for 30 min. The cell pellet was placed in a standard 5 mm NMR tube, and a 3 mm NMR tube containing the TFA/D_2O solution (0.1%) was inserted into the 5 mm tube to provide a lock signal and internal standard.

^{19}F NMR spectra of the cells were acquired at 310 K with a relaxation delay of 5 s, an acquisition time of 0.73 s, and the number of scans was 512.

The ^{19}F spin−spin (T_2) was measured using the Carr−Purcell−Meiboom−Gill pulse sequence at 310 K. The relaxation delay was 3 s, the acquisition time was 0.16 s, and the number of scans was 256. For each measurement, the echo times were varied from 2 to 770 ms and 16 points were collected.

^{19}F spin−lattice (T_1) relaxation times were measured using the standard inversion−recovery pulse sequence. The relaxation delay was 3 s, the acquisition time was 0.16 s, and the number of scans was 256. For each measurement, the recovery times were varied from 2 ms to 3 s and 16 points were acquired.

Flow Cytometry Analysis. In a 24-well plate, 50,000 cells were incubated with the dye-labeled polymers at a concentration of 0.5 mM (2.1 mg/mL of P5, 3.45 mg/mL of P10, and 5.85 mg/mL of P20). After incubation for 24 h, cells were washed twice, trypsinised, and suspended in 4% PFA/PBS solution. Cells were analyzed on a BD LSR II analyzing flow cytometer using DIVA software.

Confocal Fluorescence Microscopy. Cells were seeded onto coverslips in a 24-well plate and grown overnight at 37 °C. Then the polymer was added and incubated with cells for 24 h. Cells were fixed for 15 min in 4% PFA, before being rinsed three times in PBS and water. Cells were mounted with DAPI in Vectashield. Cy5.5 has an excitation and emission at 684 and 710 nm, respectively. DAPI has an excitation and emission at 358 and 461 nm, respectively. Cells were sealed with nail polish for confocal imaging. Images were acquired using a Zeiss LSM 710 inverted confocal microscope. Images were analyzed using ZEN software (Zeiss).

Atomistic Molecular Dynamics Simulation. MD simulations of self-assembled polymers adsorbed on the membrane were performed. The model self-assembled polymers have different numbers of monomers, P5 with eight monomers, P10 with four monomers, and P20 with one monomer. Two membrane surfaces were prepared based on a POPC (phosphatidylcholine) bilayer: M1 (perfect POPC membrane) and M2 (POPC membrane with one protrusion, which means one POPC molecule with its hydrophobic tail toward the solution). We then modeled the adsorption of the P5, P10, and P20 on the M1 and M2 membrane. In the simulations, the P5, P10, and P20 were initially placed near the outside surface of membrane M1 and above the protrusion of M2. All of the systems were placed in a 0.15 M NaCl solution. Unit cells of systems, containing P5, P10, and P20 with M1 and M2 in aqueous solution, had in total between 123,000 and 136,000 atoms.

https://dx.doi.org/10.1021/acsnano.0c02954
ACS Nano 2020, 14, 7425−7434

The polymers were described with the CHARMM general force field,[49,50] and the membranes were described with the CHARMM27 force field.[51] The simulations were performed with NAMD.[52] The particle-mesh Ewald method[53] was used for evaluation of long-range Coulomb interactions. The time step was set to 2 fs. After 2000 steps of minimization, all systems were equilibrated for 16−40 ns in the NPT ensemble (pressure p = 1 bar, temperature T = 300 K), using Langevin dynamics (γLang = 1 ps^{-1}).

Auto- and Pair-Correlation Data Analysis. One day before the actual measurement, MCF-7 cells were seeded into three dishes, which have a glass bottom with a thickness around 0.17 mm. The dishes were incubated in a cell culture incubator under 37 °C and 5% CO_2. The cell density should be approximately 70% confluent for auto/pair-correlation microscopy. On the day of measurement, the cells were washed with PBS twice, and the medium was replaced with the cell growth medium without phenol red. Then, three different types of Cy5.5-labeled polymer nanoparticles were disperseed in each dish, to have a final concentration of 20 nm, and were incubated for 4 h.

The microscope and incubation system (temperature and CO_2) of the microscope were turned on and warmed up for at least 30 min before the measurement. A drag of a 64-pixel line (pixel size = 300 nm) from extracellular space to the nucleus of the cell of interest was drawn and scanned 100,000 times with a scanning speed of 0.945 ms/line to acquire fluorescent data of the line scan.

The line scan data were analyzed with a developed MATLAB GUI (graphical user interfaces), which is available on request. The autocorrelation function ($G(\tau)$) is used to calculate the number of mobile nanoparticles traced on the selected line, which is shown as below:

$$G(t) = \frac{\langle F(t)F(t+\tau)\rangle}{\langle F(t)^2\rangle} - 1$$

where $F(t)$ is the fluorescence intensity at time t and $F(t+\tau)$ is the fluorescence intensity after a delay time, τ. $G(0)$, the amplitude of autocorrelation function at τ = 0, is used to extract the number of mobile nanoparticles (N) by using the function below:

$$N = \frac{\gamma}{G(0)}$$

where γ describes the excitation volume shape, which is 0.3536 for a one-photon point spread function three-dimensional Gaussian distribution.

To obtain the transit time of nanoparticles moving along the selected line, the fluorescence intensity of two positions on the selected line with a distance δr is calculated with pair-correlation function using the following expression as a function of delay time, τ:

$$G(\tau, \delta r) = \frac{\langle F(t, 0)F(t+\tau, \delta r)\rangle}{\langle F(t, 0)F(t, \delta r)\rangle}$$

The maximum peak of the derived pair-correlation profile gives the average time that nanoparticles take to travel the given distance.

Penetration of MCF-7 Tumor Spheroids. MCF-7 tumor spheroids were formed using the microwell-based methods published previously.[54] The devices were incubated with cell culture medium for 30 min before the cells were seeded. MCF-7 cells (400 μL) were seeded and incubated in the devices for 7 days, and the cell culture medium was replaced every 2 days. The tumor spheroids were monitored with a light microscope until the size of the tumor spheroids reached around 500 μm in diameter. The tumor spheroids were then treated with P5, P10, and P20 polymers for 24 h. After the treatment, the tumor spheroids were harvested and washed with PBS twice. They were then fixed with 4% formaldehyde for 2 h and permeabilized with 0.1% Triton X-100 in PBS for 1 h. The F-actin and nuclei of the cells were then stained with Alexa Fluor 488 Phalloidin (50 μg/mL) and DAPI (1 μg/mL) in the dark at room temperature for 1 h. After being washed, the tumor spheroids were imaged with LSM710 confocal laser-scanning upright microscopes (Zeiss).

Proliferation Assay on 2D Monolayer Cultures. MCF-7 cells were seeded into 96 well-plates in complete medium and incubated overnight to allow attachment. They were then treated with PBS control, P20, P20-CTRL + DOX, free DOX, P10 + DOX, and P20 + DOX. The IncuCyte ZOOM live-cell analysis system (Essen BioScience, Ann Ann Arbor, MI) was used to monitor real-time cell proliferation during the treatment. The proliferation curve was exported and analyzed using IncuCyte software. All experiments were replicated three times.

Anticancer Therapeutic Efficacy Using MCF-7 Tumor Spheroids. To understand the anticancer therapeutic efficacy of polymers linked with or without DOX to 3D tumor tissue spheroids, tumor spheroids were treated with PBS control, P20, P20-CTRL + DOX, free DOX, P10 + DOX, and P20 + DOX for 24 h. After fixation and washing, the tumor tissue spheroids were dehydrated, embedded in paraffin, and then cut into 5-μm-thick histologic sections. Hematoxylin and eosin (H&E) staining was performed using a Leica Autostainer XL (ST5015, Leica Microsystem, North Ryde, Australia). The stained tissue sections were analyzed by light microscopy.

Statistical Analysis. All of the experiments were repeated at least three times. The results are presented as the mean ± SD. The analysis in Figure 2 was done using the unpaired two-tailed t test analysis. One-way ANOVA analysis was used in Figure 3. A p value of less than 0.05 was considered statistically significant. Significant value p (*p < 0.05, **p < 0.01, ***p < 0.001, and ****p < 0.0001).

ASSOCIATED CONTENT

Supporting Information

The Supporting Information is available free of charge at https://pubs.acs.org/doi/10.1021/acsnano.0c02954.

Additional experimental section, structural characterizations, additional NMR spectroscopy, and MD simulations (PDF)

AUTHOR INFORMATION

Corresponding Authors

Cheng Zhang − *Australian Institute for Bioengineering and Nanotechnology and ARC Centre of Excellence in Convergent Bio-Nano Science and Technology, The University of Queensland, Brisbane, Qld 4072, Australia; Materials Research Laboratory, University of California, Santa Barbara, California 93106, United States;* orcid.org/0000-0002-2722-7497; Email: c.zhang3@uq.edu.au

Andrew K. Whittaker − *Australian Institute for Bioengineering and Nanotechnology and ARC Centre of Excellence in Convergent Bio-Nano Science and Technology, The University of Queensland, Brisbane, Qld 4072, Australia;* orcid.org/0000-0002-1948-8355; Email: a.whittaker@uq.edu.au

Authors

Tianqing Liu − *QIMR Berghofer Medical Research Institute, Brisbane, Qld 4006, Australia*

Wenqian Wang − *Australian Centre for NanoMedicine and School of Chemistry, University of New South Wales, Sydney 2052, Australia*

Craig A. Bell − *Australian Institute for Bioengineering and Nanotechnology and ARC Centre of Excellence in Convergent Bio-Nano Science and Technology, The University of Queensland, Brisbane, Qld 4072, Australia;* orcid.org/0000-0002-8986-2795

Yanxiao Han − *Department of Chemistry, University of Illinois at Chicago, Chicago, Illinois 60607, United States*

Changkui Fu − *Australian Institute for Bioengineering and Nanotechnology and ARC Centre of Excellence in Convergent Bio-Nano Science and Technology, The University of Queensland, Brisbane, Qld 4072, Australia;* orcid.org/0000-0002-2444-607X

https://dx.doi.org/10.1021/acsnano.0c02954
ACS Nano 2020, 14, 7425−7434

Hui Peng − *Australian Institute for Bioengineering and Nanotechnology and ARC Centre of Excellence in Convergent Bio-Nano Science and Technology, The University of Queensland, Brisbane, Qld 4072, Australia*

Xiao Tan − *Australian Institute for Bioengineering and Nanotechnology, The University of Queensland, Brisbane, Qld 4072, Australia*

Petr Král − *Department of Chemistry, Department of Physics, and Department of Biopharmaceutical Sciences, University of Illinois at Chicago, Chicago, Illinois 60607, United States;* orcid.org/0000-0003-2992-9027

Katharina Gaus − *Australian Centre for NanoMedicine, EMBL Australia Node in Single Molecule Science, and ARC Centre of Excellence in Advanced Molecular Imaging, University of New South Wales, Sydney 2052, Australia*

J. Justin Gooding − *Australian Centre for NanoMedicine, School of Chemistry, and ARC Centre of Excellence in Convergent Bio-Nano Science and Technology, University of New South Wales, Sydney 2052, Australia;* orcid.org/0000-0002-5398-0597

Complete contact information is available at: https://pubs.acs.org/10.1021/acsnano.0c02954

Notes

The authors declare no competing financial interest.

ACKNOWLEDGMENTS

The authors acknowledge the Australian Research Council (CE140100036, DP0987407, DP110104299, LE0775684, LE0668517, and LE0882357) and the National Health and Medical Research Council (APP1021759) for funding of this research. The Australian National Fabrication Facility, Queensland Node, is also acknowledged for access to some items of equipment. C.Z. acknowledges the National Health and Medical Research Council for his Early Career Fellowship (APP1157440) and the University of Queensland for his Early Career Researcher Grant (UQECR1720289). P.K. acknowledges the NSF Division of Materials Research Grant 1506886.

REFERENCES

(1) Metelev, V.; Zhang, S.; Zheng, S.; Kumar, A. T. N.; Bogdanov, A., Jr. Fluorocarbons Enhance Intracellular Delivery of Short STAT3-Sensors and Enable Specific Imaging. *Theranostics* **2017**, *7*, 3354−3368.

(2) Dafik, L.; Kalsani, V.; Leung, A. K. L.; Kumar, K. Fluorinated Lipid Constructs Permit Facile Passage of Molecular Cargo into Living Cells. *J. Am. Chem. Soc.* **2009**, *131*, 12091−12093.

(3) Yan, G.; Wang, J.; Zhang, P.; Hu, L.; Wang, X.; Yang, G.; Fu, S.; Cheng, X.; Tang, R. Tunable Dynamic Fluorinated Poly(orthoester)-Based Drug Carriers for Greatly Enhanced Chemotherapeutic Efficacy. *Polym. Chem.* **2017**, *8*, 2063−2073.

(4) Fu, C.; Demir, B.; Alcantara, S.; Kumar, V.; Han, F.; Kelly, H. G.; Tan, X.; Yu, Y.; Xu, W.; Zhao, J.; Zhang, C.; Peng, H.; Boyer, C.; Woodruff, T. M.; Kent, S. J.; Searles, D. J.; Whittaker, A. K. Low-Fouling Fluoropolymers for Bioconjugation and *In Vivo* Tracking. *Angew. Chem., Int. Ed.* **2020**, *59*, 4729−4735.

(5) Fu, C.; Tang, J.; Pye, A.; Liu, T.; Zhang, C.; Tan, X.; Han, F.; Peng, H.; Whittaker, A. K. Fluorinated Glycopolymers as Reduction-Responsive 19F MRI Agents for Targeted Imaging of Cancer. *Biomacromolecules* **2019**, *20*, 2043−2050.

(6) Johnson, M. E.; Shon, J.; Guan, B. M.; Patterson, J. P.; Oldenhuis, N. J.; Eldredge, A. C.; Gianneschi, N. C.; Guan, Z. Fluorocarbon Modified Low-Molecular-Weight Polyethylenimine for siRNA Delivery. *Bioconjugate Chem.* **2016**, *27*, 1784−1788.

(7) Zeng, H.; Johnson, M. E.; Oldenhuis, N. J.; Tiambeng, T. N.; Guan, Z. Structure-Based Design of Dendritic Peptide Bolaamphiphiles for siRNA Delivery. *ACS Cent. Sci.* **2015**, *1*, 303−312.

(8) Chintala, L.; Vaka, S.; Baranda, J.; Williamson, S. K. Capecitabine *versus* 5-Fluorouracil in Colorectal Cancer: Where Are We Now? *Oncol. Rev.* **2011**, *5*, 129−140.

(9) Bohm, H. J.; Banner, D.; Bendels, S.; Kansy, M.; Kuhn, B.; Muller, K.; Obst-Sander, U.; Stahl, M. Fluorine in Medicinal Chemistry. *ChemBioChem* **2004**, *5*, 637−43.

(10) Gong, P.; Zhao, Q.; Dai, D.; Zhang, S.; Tian, Z.; Sun, L.; Ren, J.; Liu, Z. Functionalized Ultrasmall Fluorinated Graphene with High NIR Absorbance for Controlled Delivery of Mixed Anticancer Drugs. *Chem. - Eur. J.* **2017**, *23*, 17531−17541.

(11) Zhang, C.; Kim, D. S.; Lawrence, J.; Hawker, C. J.; Whittaker, A. K. Elucidating the Impact of Molecular Structure on the 19F NMR Dynamics and MRI Performance of Fluorinated Oligomers. *ACS Macro Lett.* **2018**, *7*, 921−926.

(12) Onal, E.; Zhang, C.; Davarcı, D.; Isci, U.; Pilet, G.; Whittaker, A. K.; Dumoulin, F. Cyclotriphosphazene, A Scaffold for 19F MRI Contrast Agents. *Tetrahedron Lett.* **2018**, *59*, 521−523.

(13) Fu, C.; Zhang, C.; Peng, H.; Han, F.; Baker, C.; Wu, Y.; Ta, H.; Whittaker, A. K. Enhanced Performance of Polymeric 19F MRI Contrast Agents through Incorporation of Highly Water-Soluble Monomer MSEA. *Macromolecules* **2018**, *51*, 5875−5882.

(14) Fu, C.; Herbst, S.; Zhang, C.; Whittaker, A. K. Polymeric 19F MRI Agents Responsive to Reactive Oxygen Species. *Polym. Chem.* **2017**, *8*, 4585−4595.

(15) Qiao, R.; Fu, C.; Li, Y.; Qi, X.; Ni, D.; Nandakumar, A.; Siddiqui, G.; Wu, H.; Zhang, Z.; Wu, T.; Zhong, J.; Tang, S.-Y.; Pan, S.; Zhang, C.; Whittaker, M.; Engle, J.; Creek, D.; Caruso, F.; Ke, P.; Davis, T. Sulfoxide-Containing Polymer-Coated Nanoparticles Demonstrate Minimal Protein Fouling and Improved Blood Circulation. *Adv. Sci.* **2020**, DOI: 10.1002/advs.202000406.

(16) Ellipilli, S.; Ganesh, K. N. Fluorous Peptide Nucleic Acids: PNA Analogues with Fluorine in Backbone (γ-CF2-apg-PNA) Enhance Cellular Uptake. *J. Org. Chem.* **2015**, *80*, 9185−9191.

(17) Doi, Y.; Katafuchi, A.; Fujiwara, Y.; Hitomi, K.; Tainer, J. A.; Ide, H.; Iwai, S. Synthesis and Characterization of Oligonucleotides Containing 2′-Fluorinated Thymidine Glycol as Inhibitors of the Endonuclease III Reaction. *Nucleic Acids Res.* **2006**, *34*, 1540−1551.

(18) Zhao, W.; Ta, H. T.; Zhang, C.; Whittaker, A. K. Polymerization-Induced Self-Assembly (PISA) - Control over the Morphology of 19F-Containing Polymeric Nano-Objects for Cell Uptake and Tracking. *Biomacromolecules* **2017**, *18*, 1145−1156.

(19) Johnson, G.; Meijs, G. F.; Laycock, B. G.; Griffith, M. G.; Chaouk, H.; Steele, J. G. Cell Interactions with Perfluoropolyether-Based Network Copolymers. *J. Biomater. Sci., Polym. Ed.* **1999**, *10*, 217−233.

(20) Wang, M.; Liu, H.; Li, L.; Cheng, Y. A Fluorinated Dendrimer Achieves Excellent Gene Transfection Efficacy at Extremely Low Nitrogen to Phosphorus Ratios. *Nat. Commun.* **2014**, *5*, 3053.

(21) Zhang, C.; Moonshi, S. S.; Han, Y.; Puttick, S.; Peng, H.; Magoling, B. J. A.; Reid, J. C.; Bernardi, S.; Searles, D. J.; Král, P.; Whittaker, A. K. PFPE-Based Polymeric 19F MRI Agents: A New Class of Contrast Agents with Outstanding Sensitivity. *Macromolecules* **2017**, *50*, 5953−5963.

(22) Zhang, C.; Moonshi, S. S.; Wang, W.; Ta, H. T.; Han, Y.; Han, F. Y.; Peng, H.; Kral, P.; Rolfe, B. E.; Gooding, J. J.; Gaus, K.; Whittaker, A. K. High F-Content Perfluoropolyether-Based Nanoparticles for Targeted Detection of Breast Cancer by 19F Magnetic Resonance and Optical Imaging. *ACS Nano* **2018**, *12*, 9162−9176.

(23) Zhang, C.; Li, L.; Han, F. Y.; Yu, X.; Tan, X.; Fu, C.; Xu, Z. P.; Whittaker, A. K. Integrating Fluorinated Polymer and Manganese-Layered Double Hydroxide Nanoparticles as pH-activated 19F MRI Agents for Specific and Sensitive Detection of Breast Cancer. *Small* **2019**, *15*, No. 1902309.

(24) Zhang, C.; Sanchez, R. J. P.; Fu, C.; Clayden-Zabik, R.; Peng, H.; Kempe, K.; Whittaker, A. K. Importance of Thermally-Induced Aggregation on 19F Magnetic Resonance Imaging of Perfluoropolyether-Based Comb-Shaped Poly(2-Oxazoline)s. *Biomacromolecules* **2019**, *20*, 365−374.

(25) Zhang, C.; Bates, M. W.; Geng, Z.; Levi, A. E.; Vigil, D.; Barbon, S. M.; Loman, T.; Delaney, K. T.; Fredrickson, G. H.; Bates, C. M.; Whittaker, A. K.; Hawker, C. J. Rapid Generation of Block Copolymer Libraries using Automated Chromatographic Separation. *J. Am. Chem. Soc.* **2020**, DOI: 10.1021/jacs.0c04028.
(26) Liu, Y.; Zhang, C.; Liu, H.; Li, Y.; Xu, Z.; Li, L.; Whittaker, A. Controllable Synthesis of Up-Conversion Nanoparticles UCNPs@MIL-PEG for pH-Responsive Drug Delivery and Potential Up-Conversion Luminescence/Magnetic Resonance Dual-Mode Imaging. *J. Alloys Compd.* **2018**, *749*, 939−947.
(27) Liu, Y.; Zhang, C.; Xu, C.; Lin, C.; Sun, K.; Wang, J.; Chen, X.; Li, L.; Whittaker, A. K.; Xu, H. B. Controlled Synthesis of Up-Conversion Luminescent Gd/Tm-MOFs for pH-Responsive Drug Delivery and UCL/MRI Dual-Modal Imaging. *Dalton Trans.* **2018**, *47*, 11253−11263.
(28) Lin, C.; Chi, B.; Xu, C.; Zhang, C.; Tian, F.; Xu, Z.; Li, L.; Whittaker, A.; Wang, J. Multifunctional Drug Carrier on Basis of 3d-4f Fe/La-MOFs for Drug Delivery and Dual-Mode Imaging. *J. Mater. Chem. B* **2019**, *7*, 6612−6622.
(29) Pearce, A. K.; Simpson, J. D.; Fletcher, N. L.; Houston, Z. H.; Fuchs, A. V.; Russell, P. J.; Whittaker, A. K.; Thurecht, K. J. Localised Delivery of Doxorubicin to Prostate Cancer Cells through A PSMA-Targeted Hyperbranched Polymer Theranostic. *Biomaterials* **2017**, *141*, 330−339.
(30) Pearce, A. K.; Rolfe, B. E.; Russell, P. J.; Tse, B. W. C.; Whittaker, A. K.; Fuchs, A. V.; Thurecht, K. J. Development of A Polymer Theranostic for Prostate Cancer. *Polym. Chem.* **2014**, *5*, 6932−6942.
(31) Ahrens, E. T.; Helfer, B. M.; O'Hanlon, C. F.; Schirda, C. Clinical Cell Therapy Imaging Using A Perfluorocarbon Tracer and Fluorine-19 MRI. *Magn. Reson. Med.* **2014**, *72*, 1696−1701.
(32) Moonshi, S. S.; Zhang, C.; Peng, H.; Puttick, S.; Rose, S.; Fisk, N. M.; Bhakoo, K.; Stringer, B. W.; Qiao, G. G.; Gurr, P. A.; Whittaker, A. K. A Unique 19F MRI Agent for the Tracking of Non Phagocytic Cells *In Vivo*. *Nanoscale* **2018**, *10*, 8226−8239.
(33) Zhang, C.; Ferenz, K. B. Nano-Bio-Imaging and Therapeutic Nanoparticles. *J. Nanosci. Nanomed.* **2018**, *2*, 19−20.
(34) Zhang, C.; Peng, H.; Li, W.; Liu, L.; Puttick, S.; Reid, J.; Bernardi, S.; Searles, D. J.; Zhang, A.; Whittaker, A. K. Conformation Transitions of Thermoresponsive Dendronized Polymers across the Lower Critical Solution Temperature. *Macromolecules* **2016**, *49*, 900−908.
(35) Zhang, C.; Moonshi, S. S.; Peng, H.; Puttick, S.; Reid, J.; Bernardi, S.; Searles, D. J.; Whittaker, A. K. Ion-Responsive 19F MRI Contrast Agents for the Detection of Cancer Cells. *ACS Sensors* **2016**, *1*, 757−765.
(36) Zhang, C.; Peng, H.; Puttick, S.; Reid, J.; Bernardi, S.; Searles, D. J.; Whittaker, A. K. Conformation of Hydrophobically Modified Thermoresponsive Poly(OEGMA-Co-TFEA) across the LCST Revealed by NMR and Molecular Dynamics Studies. *Macromolecules* **2015**, *48*, 3310−3317.
(37) Van Lehn, R. C.; Alexander-Katz, A. Pathway for Insertion of Amphiphilic Nanoparticles into Defect-Free Lipid Bilayers from Atomistic Molecular Dynamics Simulations. *Soft Matter* **2015**, *11*, 3165−3175.
(38) Van Lehn, R. C.; Ricci, M.; Silva, P. H.; Andreozzi, P.; Reguera, J.; Voïtchovsky, K.; Stellacci, F.; Alexander-Katz, A. Lipid Tail Protrusions Mediate the Insertion of Nanoparticles into Model Cell Membranes. *Nat. Commun.* **2014**, *5*, 4482.
(39) Hinde, E.; Thammasiraphop, K.; Duong, H. T. T.; Yeow, J.; Karagoz, B.; Boyer, C.; Gooding, J. J.; Gaus, K. Pair Correlation Microscopy Reveals the Role of Nanoparticle Shape in Intracellular Transport and Site of Drug Release. *Nat. Nanotechnol.* **2017**, *12*, 81−89.
(40) Kuimova, M. K.; Botchway, S. W.; Parker, A. W.; Balaz, M.; Collins, H. A.; Anderson, H. L.; Suhling, K.; Ogilby, P. R. Imaging Intracellular Viscosity of A Single Cell during Photoinduced Cell Death. *Nat. Chem.* **2009**, *1*, 69−73.
(41) Luby-Phelps, K.; Mujumdar, S.; Mujumdar, R. B.; Ernst, L. A.; Galbraith, W.; Waggoner, A. S. A Novel Fluorescence Ratiometric Method Confirms the Low Solvent Viscosity of the Cytoplasm. *Biophys. J.* **1993**, *65*, 236−242.
(42) Baek, Y.; Park, S. J.; Zhou, X.; Kim, G.; Kim, H. M.; Yoon, J. A Viscosity Sensitive Fluorescent Dye for Real-Time Monitoring of Mitochondria Transport in Neurons. *Biosens. Bioelectron.* **2016**, *86*, 885−891.
(43) Echeverria, C.; Kapral, R. Enzyme Kinetics and Transport in A System Crowded by Mobile Macromolecules. *Phys. Chem. Chem. Phys.* **2015**, *17*, 29243−29250.
(44) Echeverria, C.; Kapral, R. Molecular Crowding and Protein Enzymatic Dynamics. *Phys. Chem. Chem. Phys.* **2012**, *14*, 6755−6763.
(45) Verkman, A. S. Solute and Macromolecule Diffusion in Cellular Aqueous Compartments. *Trends Biochem. Sci.* **2002**, *27*, 27−33.
(46) Liu, T.; Kempson, I.; de Jonge, M.; Howard, D. L.; Thierry, B. Quantitative Synchrotron X-Ray Fluorescence Study of the Penetration of Transferrin-Conjugated Gold Nanoparticles Inside Model Tumour Tissues. *Nanoscale* **2014**, *6*, 9774−9782.
(47) Zhao, J.; Lu, H.; Wong, S.; Lu, M.; Xiao, P.; Stenzel, M. H. Influence of Nanoparticle Shapes on Cellular Uptake of Paclitaxel Loaded Nanoparticles in 2D and 3D Cancer Models. *Polym. Chem.* **2017**, *8*, 3317−3326.
(48) Rao, W.; Wang, H.; Han, J.; Zhao, S.; Dumbleton, J.; Agarwal, P.; Zhang, W.; Zhao, G.; Yu, J.; Zynger, D. L.; et al. Chitosan-Decorated Doxorubicin-Encapsulated Nanoparticle Targets and Eliminates Tumor Reinitiating Cancer Stem-Like Cells. *ACS Nano* **2015**, *9*, 5725−5740.
(49) Vanommeslaeghe, K.; MacKerell, A. D. Automation of the CHARMM General Force Field (CGenFF) I: Bond Perception and Atom Typing. *J. Chem. Inf. Model.* **2012**, *52*, 3144−3154.
(50) Vanommeslaeghe, K.; Raman, E. P.; MacKerell, A. D. Automation of the CHARMM General Force Field (CGenFF) II: Assignment of Bonded Parameters and Partial Atomic Charges. *J. Chem. Inf. Model.* **2012**, *52*, 3155−3168.
(51) Feller, S. E.; Yin, D.; Pastor, R. W.; MacKerell, A. D., Jr. Molecular Dynamics Simulation of Unsaturated Lipid Bilayers at Low Hydration: Parameterization and Comparison with Diffraction Studies. *Biophys. J.* **1997**, *73*, 2269−2279.
(52) Phillips, J. C.; Braun, R.; Wang, W.; Gumbart, J.; Tajkhorshid, E.; Villa, E.; Chipot, C.; Skeel, R. D.; Kalé, L.; Schulten, K. Scalable Molecular Dynamics with NAMD. *J. Comput. Chem.* **2005**, *26*, 1781−1802.
(53) Darden, T.; York, D.; Pedersen, L. Particle Mesh Ewald: An N·Log(N) Method for Ewald Sums in Large Systems. *J. Chem. Phys.* **1993**, *98*, 10089−10092.
(54) Whatley, B. R.; Li, X.; Zhang, N.; Wen, X. Magnetic-Directed Patterning of Cell Spheroids. *J. Biomed. Mater. Res., Part A* **2014**, *102*, 1537−1547.

https://dx.doi.org/10.1021/acsnano.0c02954
ACS Nano 2020, 14, 7425−7434